Phase and micromotion of Bose-Einstein condensates in a time-averaged ring trap

Thomas A. Bell,[1],[*] Guillaume Gauthier,[1] Tyler W. Neely,[1] Halina Rubinsztein-Dunlop,[1]
Matthew J. Davis,[2] and Mark A. Baker[1]

[1]*ARC Centre of Excellence for Engineered Quantum Systems (EQuS), School of Mathematics and Physics,*
University of Queensland, Brisbane QLD 4072, Australia
[2]*ARC Centre of Excellence in Future Low-Energy Electronics Technologies, School of Mathematics and Physics,*
University of Queensland, Brisbane QLD 4072, Australia

Rapidly scanning magnetic and optical dipole traps have been widely utilized to form time-averaged potentials for ultracold quantum gas experiments. Here we theoretically and experimentally characterize the dynamic properties of Bose-Einstein condensates in ring-shaped potentials that are formed by scanning an optical dipole beam in a circular trajectory. We find that unidirectional scanning leads to a nontrivial phase profile of the condensate that can be approximated analytically using the concept of phase imprinting. While the phase profile is not accessible through in-trap imaging, time-of-flight expansion manifests clear density signatures of an in-trap phase step in the condensate, coincident with the instantaneous position of the scanning beam. The phase step remains significant even when scanning the beam at frequencies 2 orders of magnitude larger than the characteristic frequency of the trap. We map out the phase and density properties of the condensate in the scanning trap, both experimentally and using numerical simulations, and find excellent agreement. Furthermore, we demonstrate that bidirectional scanning flattens the phase profile, rendering the system more suitable for coherent matter-wave interferometry.

I. INTRODUCTION

The ability to engineer trapping potentials for ultracold quantum gases has enabled their use to study a wide range of macroscopic quantum phenomena. In the late 1990s the most commonly used potentials were relatively simple magnetic traps generated by current-carrying coils and wires [1,2], and optical dipole traps formed using few- or single-beam configurations of independent lasers [3]. Today, increasingly sophisticated traps for ultracold gases employ a range of techniques, including optical lattices [4], rf dressing of magnetic potentials [5–7], and pattern projection using spatial light modulators [8,9] or digital micromirror devices [10,11].

An important step toward the first experimental demonstration of Bose-Einstein condensates (BECs) was the development of the time-orbiting potential, or TOP trap [12]. It had previously been observed that spin-polarized atoms confined in a quadrupole magnetic trap could undergo Majorana transitions near the zero of the magnetic field. As the cloud evaporatively cooled, atoms spent more time in the vicinity of the trap minimum, increasing the rate of atom loss [13]. However, it was realized that adding a rapidly rotating bias field could solve this problem. If the field rotation frequency was fast enough that atoms did not move far during a period, but slow enough that the atomic spin could adiabatically follow the local magnetic field direction, then to a good approximation the system experienced a pseudostatic potential equivalent to the instantaneous potential time-averaged over one field

rotation period. This is conceptually similar to the oscillating electric fields used to confine ions in Paul traps [14].

TOP traps were a popular choice for many of the early experiments on ultracold gases, however, today relatively few groups make use of these potentials. One of the drawbacks of TOP traps is that the potentials are not actually static; beyond the zeroth-order approximation, there exists a micromotion of the trapped atoms. This was examined in detail experimentally by the Arimondo group in Refs. [15,16]. Challis *et al.* also presented a detailed theoretical study of micromotion in a TOP trap [17].

The same principle of time-averaging can be applied to optical dipole traps. If the laser is scanned sufficiently quickly, atoms will experience a time-averaged optical potential (TAOP) [18–21]. A variety of trapping geometries for degenerate quantum gases have been formed using this method, including line [18], ring [22], and lattice [23] potentials. The prospect of atomtronic applications, where analogs of electronic circuits for atoms are engineered, has motivated studies into persistent currents [24], integrated matter-wave circuits [25], and Josephson junctions [26]. Parallel matter-wave splitting [27] and efficient runaway optical evaporation [28] have also been demonstrated.

Our group has recently studied BECs in time-averaged traps generated by scanning an optical dipole beam using a two-dimensional acousto-optical deflector (2D-AOD), with a particular emphasis on ring-shaped traps [29]. We have developed a control algorithm that measures the atom distribution in the ring through absorption imaging and then applies an intensity correction to the scanning beam. This feedforward technique reduces the trap depth fluctuations of the ring to

*t.bell4@uq.edu.au

less than 10% rms of the chemical potential. While images of the atoms taken in-trap show a smooth atomic density profile, we observe a prominent density feature in the ring for scan frequencies of the dipole trap less than a few kHz. The coincidence of this feature with the instantaneous beam location suggests that it results from the scanning motion of the dipole beam and motivates a more careful study of micromotion in these systems. In particular, such micromotion would likely affect the BEC phase profile and therefore be detrimental to matter-wave interferometry.

In this work, we further characterize the properties of a BEC within a scanned optical ring potential and identify several features arising from the time-dependent nature of the potential. In particular, we observe density and phase features of the BEC that follow the scanned trapping beam; the latter we show may be understood using the principle of phase imprinting [30]. While the magnitude of these features can be reduced by increasing the scan frequency, they cannot be eliminated entirely. Finally, we demonstrate an adapted scan strategy that produces a more uniform azimuthal phase.

II. EXPERIMENTAL SETUP

Our experimental apparatus and procedure have been previously described in Ref. [29]. Numerous subsequent improvements are described in Appendix A. Briefly, we form ^{87}Rb BECs in the $F = 1$, $m_F = -1$ state, with atom number $N_0 \approx 2 \times 10^6$, temperature $T \approx 75$ nK, and condensate fraction $N_0/N \approx 0.85$. Our ring traps are formed by intersecting two $\lambda = 1064$-nm optical dipole traps, illustrated in Fig. 1. A cylindrical lens is used to generate a horizontal laser sheet that provides harmonic vertical confinement with $f_z = 140$ Hz; the $1/e^2$ waists are $\sigma_x = 1.25$ mm and $\sigma_z = 27$ μm. A second vertical Gaussian beam with waist $\sigma_\rho = 26.5$ μm is scanned
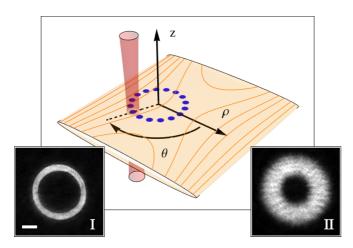

FIG. 1. Schematic of the experimental setup. The ring potential is formed by combining a red-detuned laser sheet that confines atoms in the $z = 0$ plane with a vertically propagating red-detuned beam that is rapidly scanned in the xy plane. (Insets) Experimental absorption images of the ring condensate density following feedforward correction. The images are taken after 1 ms (I) and 20 ms (II) TOF expansion and rescaled to the peak density. The ring has radius $R = 82$ μm, and the scale bar in (I) has 50 μm length.

in a circle of radius $R = 82$ μm to form a time-averaged ring trap with a radial harmonic frequency $f_\rho = 50$ Hz.

An acousto-optic deflector (AOD) scans the trapping beam at frequency f_s (IntraAction DTD-274HA6). Frequency-shift keying function generators drive the two orthogonal AOD channels independently (SpinCore Pulseblaster). This discrete scan protocol simplifies the parametrization of arbitrary-shaped potentials. We scan $p = 32$ points spaced by 0.61 σ_ρ, which gives sufficient overlap for a smooth potential while maximizing the scan frequency f_s. The AOD access time constrains $f_s \leqslant 6.25$ kHz for this configuration. In practice, the discrete scan is equivalent to continuously chirping the radio frequencies.

To improve the trap uniformity we measure the atom density following a short 1-ms time of flight (TOF) and perform an iterative feedforward correction to the p beam powers around the ring [Fig. 1(I)]. These adjustments are subsequently refined using 20 ms TOF imaging, resulting in ring BECs with uniform density within experimental uncertainties [Fig. 1(II)].

III. ANALYTICAL CONDENSATE PHASE IN TIME-AVERAGED RING TRAPS

In this section we develop an analytical description for the phase profile of the condensate held in a time-averaged ring trap. The ring potential is generated by scanning a single Gaussian beam around a circular path of radius R, with angular frequency $\omega = 2\pi f_s$. When the path curvature may be neglected ($\sigma_\rho \ll R$), the instantaneous potential can be approximated by

$$V(\rho,\theta,t) = \left(\frac{\overline{V}\sqrt{8\pi}R}{\sigma_\rho}\right)e^{-2[(\frac{\rho-R}{\sigma_\rho})^2+(\frac{R(\theta-\omega t)}{\sigma_\rho})^2]}. \qquad (1)$$

The time-averaged trap depth is

$$\overline{V} = -m\,\pi^2\sigma_\rho^2\,f_\rho^2\,, \qquad (2)$$

where m is the particle mass, σ_ρ the scan beam waist, and f_ρ the time-averaged radial trap frequency. The condensate wave function $\Psi(\rho,\theta,t)$ evolves according to the Gross-Pitaevskii equation (GPE),

$$i\hbar\frac{\partial\Psi}{\partial t} = \left(\frac{-\hbar^2}{2m}\nabla^2 + V + g|\Psi|^2\right)\Psi\,, \qquad (3)$$

where $g = 4\pi\hbar^2 a_s/m$ is the three-dimensional coupling constant and a_s the s-wave scattering length. For sufficiently large scanning frequency ω, the potential term evolves faster than the timescale over which kinetic and interaction terms evolve. We explore this limit in the following derivation by neglecting these terms in the GPE and retaining only the potential term. We express the polar wave function in the Madelung form,

$$\Psi(\rho,\theta,t) = \sqrt{n(\rho,\theta,t)}\,e^{-i\,\phi(\rho,\theta,t)}\,. \qquad (4)$$

Substituting Eq. (4) into Eq. (3), then collecting imaginary terms,

$$\frac{\partial\,n(\rho,\theta,t)}{\partial t} = 0\,. \qquad (5)$$

The initial density profile thus remains constant in time within this approximation; we therefore adopt a Thomas-Fermi

density for the time-averaged potential [31]. The Thomas-Fermi radius R_ρ and chemical potential μ are given by

$$R_\rho = \sqrt{\frac{\mu}{2m\pi^2 f_\rho^2}} \quad , \quad \mu = \sqrt{\frac{2Ng\,mf_\rho f_z}{R}} \, . \tag{6}$$

Collecting real terms gives the equation of motion for the condensate phase,

$$\hbar \frac{\partial \phi(\rho,\theta,t)}{\partial t} = V(\rho,\theta,t) \, , \tag{7}$$

which shows the trapping beam continuously imprints the condensate phase while scanning [30]. Solving Eq. (7) using Eq. (1), the condensate phase is

$$\phi = \frac{\delta_\phi}{2}\left[\kappa - \mathrm{erf}\left(\frac{\sqrt{2}\,R(\theta-\omega t)}{\sigma_\rho}\right)\right]e^{-2(\frac{\rho-R}{\sigma_\rho})^2}, \tag{8}$$

where we define the phase step

$$\delta_\phi = \left(\frac{\overline{V}}{\hbar f_s}\right). \tag{9}$$

The integration constant $\kappa(\rho,\theta,t)$ must satisfy the periodic phase and velocity boundary conditions

$$\phi(\rho,\theta+2\pi,t) = \phi(\rho,\theta,t) + 2\pi q \, , \tag{10}$$

$$\vec{v}(\rho,\theta+2\pi,t) = \vec{v}(\rho,\theta,t) \, . \tag{11}$$

The condensate velocity is defined by

$$\vec{v}(\rho,\theta,t) = \left(\frac{-\hbar}{m}\right)\nabla\phi(\rho,\theta,t) \, , \tag{12}$$

and the integer winding number q accounts for a persistent flow. Toward solving these boundary conditions, we use

Eqs. (8) and (12) to compute the polar velocity field:

$$\vec{v}(\rho,\theta,t) = \left(\frac{\hbar\,\delta_\phi}{2m}\right)\exp\left(\frac{-2(\rho-R)^2}{\sigma_\rho^2}\right)$$

$$\times \left\{\frac{4(\rho-R)}{\sigma_\rho^2}\left[\kappa - \mathrm{erf}\left(\frac{\sqrt{2}R(\theta-\omega t)}{\sigma_\rho}\right)\right]\hat{\rho}\right.$$

$$\left.+ \frac{1}{\rho}\left[\sqrt{\frac{8}{\pi}}\frac{R}{\sigma_\rho}\exp\left(\frac{-2R^2(\theta-\omega t)^2}{\sigma_\rho^2}\right) - \frac{\partial\kappa}{\partial\theta}\right]\hat{\theta}\right\}. \tag{13}$$

An integration constant of the form

$$\kappa(\rho,\theta,t) = \left[\frac{1}{\pi} + \left(\frac{2q}{\delta_\phi}\right)e^{2(\frac{\rho-R}{\sigma_\rho})^2}\right](\theta-\omega t) + \kappa_0 \tag{14}$$

satisfies Eqs. (10) and (11) for any constant κ_0. While nonlinear solutions in θ are possible, they do not minimize the system energy. We hereon let $q = 0$ for simplicity. For the BEC to have zero time-averaged velocity, $\kappa_0 = 0$. For κ_0 greater (less) than zero the mean radial velocity monotonically decreases (increases) with displacement $|\rho - R|$.

The imprinted BEC phase solution described by Eq. (8) is visualized in Fig. 2(a) for $\kappa_0 = 0$. The profile $\phi(R,\theta)$, shown at three subsequent times, demonstrates the phase step δ_ϕ advances with the trapping beam. The two-dimensional (2D) phase profile is shown in Fig. 2(b). Beyond the Thomas-Fermi approximation, the condensate will respond to the associated velocity field and confined particles will undergo micromotion. Using Euler integration, we solve Eq. (13) to trace four single-particle paths in Fig. 2(d). These open orbits induce net movement around the ring, biasing one propagation direction for interferometric applications [29]. This may serendipitously provide a scan-frequency-controlled calibration mechanism; the scan direction may be reversed or the frequency changed.
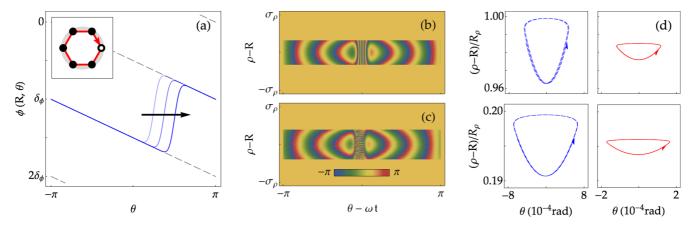

FIG. 2. Analytical solutions for the phase of the unidirectionally scanned ring condensate. (a) Snapshots at three equally spaced times of the azimuthal phase profile of the BEC in the scanned ring trap, at $\rho = R$. The phase step δ_ϕ advances with the scanning beam location. The black arrow indicates the direction of beam motion. (Inset) Schematic of the unidirectional scan ordering. Black dots represent the discrete scan locations around the ring, commencing at $\theta = 0$ (open circle). The red arrow shows the scan order. (b) Density plot of the analytical phase solution [Eq. (8)] for scan frequency $f_s = 0.5$ kHz. The phase is shown for $|\rho - R| < R_\rho$. (c) Density plot of the numerical phase solution, for the same parameters as (b) and as discussed in Sec. IV. (d) Particle trajectories which illustrate the amplitude of micromotion within the time-averaged trap for scan frequencies $f_s = 0.5$ kHz (blue dashed) and $f_s = 6.25$ kHz (red solid). The resulting micromotion is plotted over three scan cycles for initial radial positions R_ρ (top) and $0.2R_\rho$ (bottom). The amplitude of the azimuthal and radial motion reduces at higher scan frequency.

IV. NUMERICAL CONDENSATE SOLUTION IN TIME-AVERAGED RING TRAPS

In this section we use numerical simulations of the GPE to characterize the dynamics of condensates in time-averaged ring traps [32]. These results confirm the analytical predictions from Sec. III and show a density feature accompanying the phase step which also moves with the scanning beam. An extended discussion regarding the necessary scan frequency and trap parameters for stable time-averaged confinement is provided in Appendix B.

The three-dimensional simulation of the GPE is a numerically demanding task. While it is feasible to find the ground state for a static 3D potential, and even to simulate dynamics of the system following a disturbance, it is extremely challenging to fully simulate a 3D-BEC in a scanning trap where there is a significant separation of time scales between the scanning frequency and the typical trap frequencies, or in time-of-flight expansion where a significant spatial domain is required. We have therefore developed an approximate 2D reduction of the GPE to find both the state of the system in the scanning trap and to simulate the expansion dynamics in time of flight. Full details of this methodology will be discussed elsewhere.

Our two-dimensional simulations proceed by initially finding the ground-state BEC for a static ring potential. The condensate is then adiabatically transferred over 50 scan periods to a scanning potential that is equivalent to the static ring when time averaged. Our numerics replicate the discrete scanning of the ring potential in the experiment as described in Sec. II; however, we note that simulations with a continuously scanned beam produced no discernible difference.

The numerical simulations result in condensate phase profiles with identical shape and step δ_ϕ to the analytical result [Figs. 2(b) and 2(c)]. However, as the kinetic energy term is now included, the numerical density is nonuniform. We find that the normalized azimuthal density profile

$$\chi(\theta,t) = \frac{2\pi \, n(R,\theta,t)}{\int_0^{2\pi} n(R,\theta,t)\,d\theta} \qquad (15)$$

rotates with the beam and phase profile (Fig. 3); the minimal density point coincides with the instantaneous beam location. Through numerical data regression, we find the normalized density step is

$$\delta_\chi = \gamma \left(\frac{f_\rho}{f_s} \right)^2, \qquad (16)$$

where parameter $\gamma = 5.5 \pm 0.6$. The size of the density step decreases with increasing scan frequency as the limit for time-averaged confinement is approached. The effect of the scan-driven dynamics within TAOP will have implications for phase-sensitive applications such as matter-wave interferometry. One approach to mitigate imprinted phase structure is demonstrated in Sec. VI.

While the phase profile of BECs in unidirectionally scanned ring potentials may complicate measurements in proposed interferometry schemes, the phase imprinting of the scanned beam could be utilized in other situations. For example, we have simulated the generation of persistent currents with up to 8π phase windings using ideas related to those recently described in Ref. [33]. We commence with a BEC that is
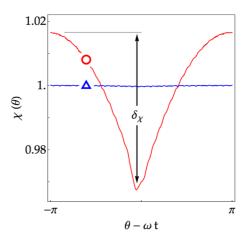

FIG. 3. Normalized angular density profiles $\chi(\theta)$ from GPE simulations for scan frequencies $f_s = 6.25$ kHz (triangle) and $f_s = 0.5$ kHz (circle) before time-of-flight expansion. Experimental values for the vertical trap frequency $f_z = 140$ Hz, radius $R = 82\ \mu$m, and atom number $N_0 = 2 \times 10^6$ are used. The definition of the density step δ_χ is indicated.

initially confined within a time-averaged ring trap that is broken using a repulsive barrier potential to realize a simply connected condensate. Commencing at the barrier, the trapping beam then performs a single unidirectional scan with linearly increasing power around the ring before returning to the usual scanning pattern. This procedure phase imprints a current on the BEC. The barrier beam then moves with the induced current as it is slowly removed over a quarter period. A persistent current is formed when the BEC reconnects. An additional manoeuvrable barrier is required before we implement this protocol experimentally.

V. COMPARISON OF NUMERICAL AND EXPERIMENTAL RESULTS

In this section we compare the results of numerical GPE simulations with our experimental observations of condensates in time-averaged traps. Through time-of-flight expansion, condensate phase features transform into density features [34], which can be observed using absorption imaging. In our experiment, we use the atom density profile in time of flight to correct azimuthal trap depth nonuniformities. This unfortunately complicates the interpretation of single absorption images, as any residual corrugations in the trapping potential cannot be readily distinguished from the density features arising from the phase profile. Our solution is to average a sequence of absorption images taken with an incremented final scanning beam location. The average of these images accumulates the phase-induced feature that coincides with the known final position of the scanning beam. Stationary features are conversely removed through averaging; see Appendix C for complete details.

In Fig. 4(a) we compare experimental images of BECs in time-averaged ring potentials scanned at frequencies $f_s = 0.5$ kHz and 6.25 kHz. For these measurements $N_0 = 2 \times 10^6$, radius $R = 82\ \mu$m, waist $\sigma_\rho = 26.5\ \mu$m, and radial trap frequency $f_\rho = 50$ Hz. The numerical phase and density steps are $\{\delta_\phi, \delta_\chi\} = \{15.1\pi, 5.4 \times 10^{-2}\}$ and
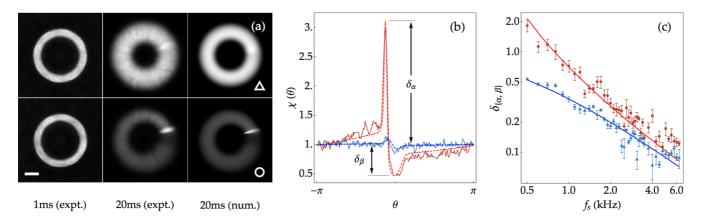
FIG. 4. Consequences of the condensate phase profile within time-averaged optical ring potentials. (a) Mean experimental absorption images for scan frequencies $f_s = 6.25$ kHz (triangle) and $f_s = 0.5$ kHz (circle), taken after 1- and 20-ms time-of-flight expansion. Imaging noise at 1-ms expansion obscures the numerically predicted density step, and the images are experimentally indistinguishable. Following 20-ms expansion, the change in the condensate for different scan rates becomes apparent and agrees with the numerical simulation results. The trapping beam was unidirectionally scanned in a clockwise direction, and the scale bar has 50-μm length. (b) Normalized angular density profiles $\chi(\theta)$ for the 20-ms TOF images in (a). The profile asymmetry motivates the definition of peak δ_α and trough δ_β amplitudes. Experimental (solid) and numerical (dashed) profiles are overlaid. (c) A comparison of experimental density peaks (red circles) and troughs (blue triangles) with simulations (solid lines). The AOD access time limits the scan frequency to $f_s \leqslant 6.25$ kHz for our ring geometry, while for frequencies $f_s \leqslant 0.5$ kHz the atoms are not confined.

$\{1.2\pi, 3.5\times10^{-4}\}$ for the respective scan frequencies. We note the phase step ($\delta_\phi > \pi$) is significant even for scan frequencies 2 orders of magnitude higher than the trap frequency.

For short time of flight (1 ms), the phase structure of the condensate has not yet affected the density, and the images are close to the in-trap density. The density profiles $\chi(\theta)$ for both scan frequencies are uniform, and indistinguishable, as the image noise exceeds the anticipated density step δ_χ. However, after 20 ms time of flight, the initial phase profile leads to an appreciable peak in the density coincident with the scanning beam location. While most pronounced for $f_s = 0.5$ kHz, the feature remains observable at 6.25 kHz, where $f_s = 125 f_\rho$. Our simulations support these observations.

Figure 4(b) compares the normalized numerical and experimental density profiles for $f_s = 0.5$ kHz (red) and $f_s = 6.25$ kHz (blue), showing excellent agreement. The density profiles can be characterized using the peak δ_α and trough δ_β amplitude, as defined in Fig. 4(b). At slow scan frequencies, there is an asymmetry in the time-of-flight density profile ($\delta_\alpha > \delta_\beta$), which reduces at higher scan frequencies. The experimental measurements of these quantities over a broad range of scan frequencies are compared with simulations in Fig. 4(c), again showing excellent agreement.

VI. BIDIRECTIONAL SCANNING

In the above analysis, we have shown that the time-averaged ring trap formed from unidirectional scanning results in a nonuniform phase profile that moves with the scanning beam. While the time-averaged imprinted velocity is vanishing, the scanning beam results in BEC micromotion for all scan frequencies. Furthermore, the phase profile becomes visible in the density through time-of-flight expansion. For most applications a more uniform phase profile in the trap is desirable, and in this section we describe a more complex scanning protocol that achieves this goal.

Rather than unidirectionally scanning a single beam around the ring [Fig. 2(a)], we consider a scheme where the trap is formed by the time average of two counter-rotating beams. This *bidirectional* scanning is schematically shown in Fig. 5(I). Each scanning beam will individually imprint a phase profile, as described by Eq. (8), but with opposite gradient. The sum of these profiles results in uniform phase plateaus, aside from those at the beam locations. The azimuthal phase is entirely uniform when the beams coincide after each complete scan period.

We approximate this bidirectional scheme in our system, using a single beam, by *raster* ordering the scan points, as shown in Fig. 5(II). This ordering alternates between points across the ring before reversing direction and returning to the initial position. For this alternative ordering the minimum scan frequency has increased to $f_s \geqslant 0.7$ kHz. Using $f_s = 6.25$ kHz, the phase profile in Fig. 5(a) is approximately uniform after each complete period.

Since the raster ordering shares one beam between two locations, there is a time delay between the counter-rotating periods equal to the scan point time. This produces two residual phase steps with amplitude δ_0 and located where the beams pass at $\theta = \{0, \pi\}$. For the scan frequency $f_s = 0.7$ kHz, these steps in Fig. 5(b) are significant but may be neglected for $f_s = 6.25$ kHz in Fig. 5(c). For both cases the phase step amplitude δ_ϕ exceeds the density amplitude δ_0; the relative amplitudes are $\delta_0/\delta_\phi = 0.253$ and 0.013, respectively.

In Fig. 6 we show images of the BEC in the raster-scanned trap following 20 ms TOF expansion, at three times through the scan period. We find that two density features are visible at the beam locations [Figs. 6(I) and 6(II)]. After a complete raster scan period these features are absent, producing approximately uniform phase and density [Fig. 6(III)]. The density using unidirectional scan ordering shows one rotating phase step [Fig. 6(IV)]. For the raster scan, another saddlelike density artefact manifests through the image-processing method
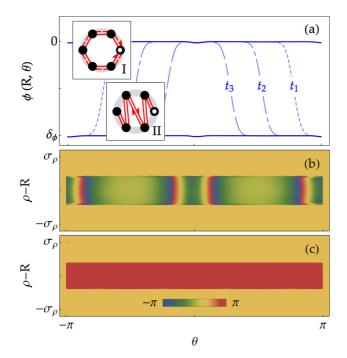
FIG. 5. Numerical data for the phase profile of the raster-scanned ring condensate. (a) Snapshots of the central phase profile, for the raster-type scan, with $f_s = 6.25$ kHz. The phase profiles at $\{t_1, t_2, t_3\}$ illustrate fractional times $\{0.25, 0.5, 0.75\}$ through the scan period showing the azimuthal expansion of a flat phase region. The phase profile is uniform at the end of each full scan period. (Inset) (I) Schematic of the idealized *bidirectional* time-averaged scan, with two beams counter-rotating. (II) The *raster* scan ordering approximates the bidirectional scan. Black dots represent the discrete points around the ring and open circles the starting locations. The red arrows show the scan orders. (b) Density plot for the $f_s = 0.7$ kHz phase profile after a complete period. The solution is radially truncated where the density becomes vanishing. Residual phase steps, with amplitude δ_0 and located at $\theta = \{0, \pi\}$, result from the temporal offset between the effective scan periods. (c) Density plot as in (b) for $f_s = 6.25$ kHz. The residual phase steps are negligible for our fastest experimental scan speeds.
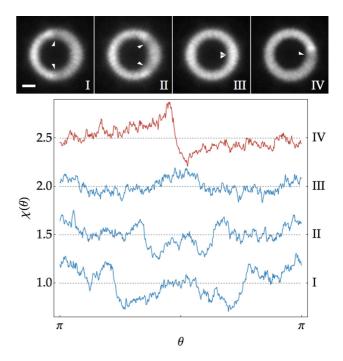

FIG. 6. Experimental density images for a bidirectionally scanned trap with frequency of $f_s = 0.7$ kHz following 20-ms TOF. (I–III) Images taken at fractional times $\{0.5, 0.75, 1\}$ through the raster scan period. White arrows indicate the instantaneous beam locations. After one complete period the phase-induced density features are absent. (IV) Comparative density using unidirectional scan ordering. The scale bar in (I) has 50-μm length. The corresponding normalized density profiles $\chi(\theta)$ are vertically displaced for visual clarity.

developed to extract phase information; see Appendix C. This stationary artefact results from the unequal amplitude modulation of scan points about the ring, inherent to the raster scan ordering, and is unrelated to the residual phase steps in Fig. 5(b). We numerically model the BEC expansion from a raster-scanned potential including this artefact and find excellent agreement; see Appendix D.

Other scanning protocols have been considered but have no obvious advantages over the unidirectional and bidirectional schemes we have described. One possibility is a random scanning pattern among the finite number of points on the ring. However, every "pulse" of the scanning beam imprints a significant phase gradient across the atoms at that location, leading to large currents for a period of time. A unidirectional scan ordering produces micromotion with the smallest amplitude by minimizing the time all locations experience the maximum gradient. The raster scan ordering approximates the bidirectional scheme and minimizes the number and amplitude of the residual defects δ_0.

A second possibility is that instead of using a fixed number of beam locations for the unidirectional scan, we could choose a step size around the ring that was incommensurate with the circumference so that the exact beam locations were never repeated. This would potentially help smooth out trap corrugations, but the phase step moving around the ring in the BEC would remain. Such a scheme would be difficult to combine with our feedforward methods, as it would significantly increase the number of registers p requiring correction to maintain uniform trap depth.

We have shown the bidirectional raster scan ordering results in significantly more uniform phase profiles over unidirectional ordering. Combined with our feedforward density correction protocol, the raster ordering produces rings with more uniform density and phase.

VII. CONCLUSIONS

In this paper we have characterized the phase properties and micromotion of Bose-Einstein condensates within ring potentials formed by rapidly scanning an optical dipole potential. In the limit of rapid scanning, we have shown that condensate dynamics result from local imprinting by the scanned beam, and we have developed an approximate analytical expression for the resulting phase profile that is in good agreement with GPE simulations.

The phase profile for unidirectional scan ordering results in a clear density feature in time-of-flight expansion that

is observable even for scan rates that are much larger than any trapping frequency. These phase and density steps are coincident with the instantaneous trapping beam position and will have consequences for using such potentials as waveguides for coherent matter waves. We have therefore subsequently developed a bidirectional raster scan ordering that periodically gives a condensate phase profile that is essentially uniform, making our system more suitable for applications such as atom interferometry [35].

APPENDIX A: CONDENSATE PRODUCTION

In our previous work, we observed two undesirable density structures around the BEC ring after time of flight (TOF), shown in Figs. 7(b) and 7(c) of Ref. [29]. Density corrugations were invariably observed, accompanied by one larger fringe at the scan beam location. We here refine our experimental
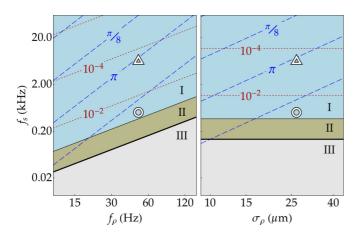

FIG. 7. Numerical mapping of three distinct regions of BEC behavior within unidirectionally scanned ring traps for scan frequency f_s, radial trap frequency f_ρ, and scan beam waist σ_ρ. The vertical trap frequency $f_z = 140$ Hz, radius $R = 82$ μm, and atom number $N_0 = 2 \times 10^6$. The regions are as follows: (I) experimentally accessible *confined* region; (II) *transition* region where the time-averaged condition begins to fail; and (III) *untrapped* region where atoms are numerically unconfined. Region boundaries are defined where trapped density profiles demonstrate irregularity (I and II) and phase profiles randomize (II and III); see Supplemental Material [39]. The contours indicate the phase step δ_ϕ (dashed) and density step δ_χ (dotted). The white circle and triangle mark the parameters for data presented in Figs. 3 and 4.

procedure to remove the corrugations, thereby enabling our current investigation into the scan dynamics. Our improved experimental method produces greater atom number, and induces fewer excitations during the ring loading and BEC phase transition, producing Figs. 1(I) and 1(II) and enabling the research of Sec. V.

Ring loading. Initially we prepare a magneto-optical trap of ^{87}Rb with $N = 2 \times 10^9$ atoms. We then transfer approximately 60% of these to a quadrupole magnetic trap in the hyperfine $F = 1$, $m_f = -1$ state, using a field gradient $dB/dz = 1.6$ T/m. We use rf evaporation to cool the cloud to the temperature $T \approx 5$ μK before lowering the magnetic field gradient to 0.29 T/m and loading the atoms into a single-beam, red-detuned dipole trap ($\lambda = 1064$ nm, $\sigma = 65$ μm) [36]. In our previous work, we evaporated further in this hybrid optical-magnetic trap and then transferred a BEC into the time-averaged ring potential [29]. In our improved scheme, we halt the evaporation after transfer to the hybrid trap. We simultaneously ramp up the intensity in the optical sheet potential and scanning ring potential while reducing the single dipole beam power and magnetic field gradient. The edge of the ring overlaps with the position of the cold thermal cloud, and the BEC forms during loading into the ring. We evaporate further by reducing the sheet beam power to increase the condensate fraction, resulting in BEC of $N_0 \approx 2 \times 10^6$ atoms at a temperature of $T \approx 75$ nK, and with $N_0/N \approx 0.85$ condensate fraction. By loading the ring from the thermal cloud, we increase the atom number in the ring considerably, while minimizing excitations.

Trap corrugations. We have reduced the spacing of the scan beam points around the ring from 0.70 σ_ρ to 0.61 σ_ρ, where σ_ρ is the $1/e^2$ waist of the scanning beam. This reduces the theoretical amplitude of depth corrugations around the ring potential by an order of magnitude. We note our value is substantially greater than the spacing of 0.31 σ_ρ needed for $p = 32$ irresolvable points according to the Sparrow criterion [37]. We consequently find the Sparrow criteria to be unnecessarily conservative in practice for our configuration. Any residual corrugations in the condensate density are not visible even after TOF expansion.

Coherence of the BEC. The atom numbers of the ring BECs are sufficiently large that they are not in the phase-fluctuating regime according to the criterion

$$N_0 > \frac{m \, k_B \, T \, \pi^2 R^2}{\hbar^2},\tag{A1}$$

which we derive from Eq. (48) of Ref. [38]. Satisfying Eq. (A1) ensures the coherence length exceeds the farthest separation between two points within the ring condensate, which is half the circumference. For temperature $T = 75$ nK and radius $R = 82$ μm, the ring BEC is fully phase coherent for $N_0 > 9 \times 10^5$ atoms.

Improved feedforward. As previously reported [29], we correct imperfections in the ring potential by measuring the atom density distribution from a series of absorption images and apply iterative corrections to the scanning beam power at each point on the ring. We previously imaged the ring condensate for 1-ms time-of-flight expansion and applied corrections to the beam power inferred from the atom distribution. We have found substantial improvement is possible by using a longer 20-ms

TOF expansion. The longer expansion time of the ring reduces the absolute optical density, broadens the available image area, and makes residual density corrugations in the trap more apparent, which can then be more accurately corrected. Absorption images are formed on a CCD camera (ProSilica EC1380) with magnification $M = 6.38$, and 1.7-μm resolution. An infinity-corrected objective is mechanically refocussed using a micrometer translation stage between images at different TOF. Although our imaging objective has been designed to correct for the cell glass thickness, in practice the objective to cell glass separation has minimal effect on the stated resolution, allowing us to mechanically move the imaging objective ~ 2 mm (for 20-ms TOF) while retaining high imaging resolution.

APPENDIX B: EXTENDED NUMERICAL ANALYSIS

Our numerical simulations have probed the properties of BECs confined by unidirectionally scanned time-averaged ring potentials over a broad parameter space. We here summarize our findings, providing guidance for the future design of new time-averaged trapping potentials and ring-based Sagnac atom interferometers.

Confinement region. From the simulations we have identified three distinct regions of behavior, summarized in Fig. 7. In region I, the *confined* region, the scan frequency f_s is sufficiently high that the condensate remains trapped following transfer to the scanning potential and is well described by the time-averaged potential. In region II, the *transition* region, as the scan frequency f_s is reduced, the time-averaged condition begins to break down. The numerical simulations show atoms being lost from the scanning potential; as visualized in the supplemental video [39]. We do not experimentally observe trapping in this region. Finally, as the scanning frequency is further decreased, the system crosses into region III, the *untrapped* region, where no confinement is provided by the time-averaged ring. The simulations show the phase step δ_ϕ, density step δ_χ, and the region boundaries are all independent of f_z, R, g, and N_0.

Confinement boundary. Outside region (I), the kinetic energy term of the GPE cannot be neglected. Given the region boundaries are independent of g and N_0, they must be determined by single-particle physics. We therefore define the kinetic energy per particle

$$K(\rho, \theta, t) = \left(\frac{-\hbar^2}{m} \right) \frac{\Psi^* \nabla^2 \Psi}{\Psi^* \Psi} \tag{B1}$$

by numerically dividing the kinetic energy density by the number density. The maximal kinetic energy K_0 occurs at the center of the scanning beam. The (II–III) region boundaries in Fig. 7 coincide with where K_0 equals the time-averaged depth $\bar{V}$ [Eq. (2)], defining the maximal density step $\delta_{\chi 0} \approx 1.5$. For $\delta_\chi = 1.5$, the minimal density in Fig. 3 drops to zero. Since the density must remain positive, the limit $\delta_\chi \ll \delta_{\chi 0}$ is physically well justified. From Eq. (16), the minimal scan frequency

$$f_s \gg \sqrt{\frac{\gamma}{\delta_{\chi 0}}} f_\rho \approx 2 f_\rho. \tag{B2}$$

Radial parametric driving induces the loss within region II. Although we have restricted our analysis to a ring geometry, the kinetic energy arguments may provide guidance

for determining the scan requirements in other time-averaged configurations, including anharmonic and uniform potentials [11].

APPENDIX C: ROTATIONALLY ACCUMULATED MEAN DENSITY IMAGES (RAMDI)

Time-of-flight absorption images of the ring BEC may have nonuniform azimuthal density features contributed from two sources. Confined density features, caused by residual trap depth corrugations, produce stationary TOF density features. The imprinted phase profile produces additional TOF density features which rotate with the scanning beam. Our method for extracting only the rotating features is described here.

Performing feedforward after expansion adapts the trap depth to compensate both contributions. Static trap depth features are therefore actively introduced by the feedforward algorithm to compensate the rotating features. These features, however, overlap and cancel only for specific hold times (Fig. 8). RAMDI are designed to extract only the rotating features by averaging out the unwanted static features.

After performing feedforward at the final beam location [Fig. 8(I)], a series of TOF images are taken with the location incremented through a subset of scan points around the ring,
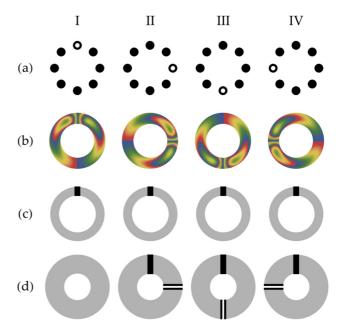

FIG. 8. Schematic of the unidirectional scanning features which motivate the rotationally accumulated mean density image (RAMDI) approach. (a) Black dots represent the discrete points scanned by the trapping beam. The open circle indicates the beam position prior to TOF imaging. Feedforward is performed after TOF and with beam position (I). For increasing hold times (II–IV), the scan beam position increments around the ring. (b) Phase profiles in trap. (c) Density profiles in trap. Markers indicate the orientation of density features induced through feedforward. These stationary features are stored in the scan beam point powers. (d) Density profiles after TOF. Markers orientate features resulting from the in-trap phase (striped) and density (solid). Feedforward with beam position (I) induces the density features (c) to correct phase features (b); they consequently cancel for this beam position only.

Figs. 8(I)–8(IV). In postprocessing, each image is rotated so the final beam locations coincide before averaging. Scan-induced features are therefore now added constructively. Stationary features are instead distributed around the ring and removed through averaging. Mean images also reduce the noise within the extracted density profiles. Given our 20-μs experimental timing resolution and 5-μs AOD limited point time, eight image series were adopted for $p = 32$ rings.

APPENDIX D: RASTER SCAN RAMDI SADDLE ARTEFACT

Using the RAMDI technique described in Appendix C, we isolate the phase-induced TOF density features for time-averaged traps formed with unidirectional ordering. Unfortunately, for the raster scan, the atomic-density-based feedforward technique is orientation dependent; the feedforward corrections change for different initial starting locations. When the RAMDI technique is applied to rings with raster scan ordering, there is an additional saddlelike density artefact which cannot readily be isolated from the phase contribution. This arises from the unequal amplitude modulation frequency of points around the ring and is unrelated to the rotating phase features. We examine this effect in detail here.

Our time-averaged optical potentials are created by frequency-shift keying the inputs to a dual-axes AOD, thereby discretely displacing the Gaussian trapping beam focus. Each point around the ring is defined using two synchronously amplitude-pulsed radio waves, or equally, two frequency combs in Fourier space. Given the mapping between radio-frequency and beam position, each single-point potential is more accurately described by convolving the 2D frequency comb with the Gaussian beam focus in position space. Single-point frequency combs broaden with increasing scan frequency f_s, forming comparatively broader and lower intensity trapping sites.

For the unidirectional scan ordering, the beam positions are all amplitude modulated using a $1/p$ duty-cycle pulse envelope, where p is the number of scan points around the ring. The points are therefore all equally broadened for all scan frequencies; the time-averaged trap depth remains inherently uniform. Consequently, our experimental feedforward scheme does not introduce depth features that are scan orientation dependent.

Since the raster scan ordering approximates two counter-rotating beams, in this situation the amplitude modulation is no longer the same for each point. Points which commence the cycle are pulsed with twice the duration and half the frequency of points an angle $\pi/2$ radians around the circumference. The relative point broadening varies both around the ring and with scan frequency. The experimental feedforward procedure now results in trap depth features to compensate for the inherently nonuniform time-averaged trap depth, for one scan orientation specifically. The BEC density is saddled in most raw images forming RAMDI, both in 1- and 20-ms TOF images, resulting in the density artefacts shown in Fig. 6.

Both the nonuniform scan point broadening and the subsequent amplitude feedforward are important when modeling the RAMDI saddle artefact for raster-scanned rings. Our approach
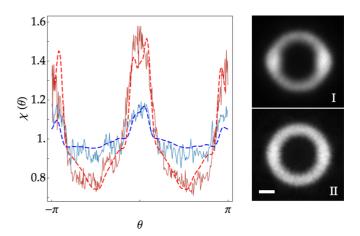

FIG. 9. Diagnostic data for the raster scan ordering RAMDI saddle artefact. Normalized density profiles for experimental RAMDI (solid), taken for 20-ms TOF, and scan frequencies $f_s = 1.25$ kHz (I) and $f_s = 0.7$ kHz (II). The numerical curves are overlaid (dashed) and computed according to the description in Appendix D. The excellent agreement indicates that saddling observed experimentally does not result from the residual phase steps δ_0 in Fig. 5(b). The depth of the saddle artefact increases with increasing scan frequency, while the residual phase steps decrease in amplitude. The scale bar in (II) has 50 μm length.

is as follows. The potential corresponding to the broadened scan points around the ring are computed by convolving the Gaussian beam with a 2D frequency comb consisting of $(2r + 1)^2$ peaks. Each comb is truncated at the first common node, which occurs at $r = 2p$. For the time-averaged potential of these broadened points we determine the amplitude correction that would produce a uniform trap depth. The inverse correction is then applied to mimic the orientation during RAMDI. The time-averaged potential then consists of the sum of scan points with uneven breadth and power. We compare the resulting experimental density with GPE simulations of the BEC in the uneven trap following 20 ms TOF in Fig. 9, showing excellent agreement. The depth of the saddle artefact increases with the scan frequency, in contrast to the decrease in the amplitude of the residual phase steps in Fig. 5(b).

Using alternative nomenclature, the diffracted orders which surround each amplitude-modulated central point frequency are "ghost" beams, a generic name which describes any beam produced unintentionally. Ghost beams are encountered when simultaneously driving a single AOD crystal with multiple frequencies [27]. These multiplexed inputs produce ghost beams corresponding to the sum and difference frequencies. Forming time-averaged potentials through chirping singular drive frequencies avoids this particular circumstance. Ghost beams may, however, alternatively arise within multidimensionally scanned systems that are not accurately synchronized [40]. We introduce a trigger pulse delay between the two SpinCore function generators. This accounts for the transmission delay and synchronizes the AOD outputs to within the 80-ns trigger latency. Ghost beams of this variety grow with increasing scan frequency but remain negligible for our fastest scan frequencies.

[1] T. Esslinger, I. Bloch, and T. W. Hänsch, Phys. Rev. A **58**, R2664 (1998).

[2] J. Fortagh, A. Grossman, C. Zimmerman, and T. W. Hänsch, Phys. Rev. Lett. **81**, 5310 (1998).

[3] R. Grimm, M. Weidemüller, and Y. B. Ovchinnikov, Adv. At. Mol. Opt. Phys. **42**, 95 (2000).

[4] I. Bloch, Nat. Phys. **1**, 23 (2005).

[5] O. Zobay and B. M. Garraway, Phys. Rev. Lett. **86**, 1195 (2001).

[6] Y. Colombe, E. Knyazchyan, O. Morizot, B. Mercier, V. Lorent, and H. Perrin, EPL **67**, 593 (2004).

[7] T. Schumm, S. Hofferberth, L. M. Andersson, S. Wildermuth, S. Groth, I. Bar-Joseph, J. Schmiedmayer, and P. Krüger, Nat. Phys. **1**, 57 (2005).

[8] V. Boyer, R. M. Godun, G. Smirne, D. Cassettari, C. M. Chandrashekar, A. B. Deb, Z. J. Laczik, and C. J. Foot, Phys. Rev. A **73**, 031402 (2006).

[9] T. A. Haase, D. H. White, D. J. Brown, I. Herrera, and M. D. Hoogerland, Rev. Sci. Instrum. **88**, 113102 (2017).

[10] C. Muldoon, L. Brandt, J. Dong, D. Stuart, E. Brainis, M. Himsworth, and A. Kuhn, New J. Phys. **14**, 073051 (2012).

[11] G. Gauthier, I. Lenton, N. M. Parry, M. Baker, M. J. Davis, H. Rubinsztein-Dunlop, and T. W. Neely, Optica **3**, 1136 (2016).

[12] W. Petrich, M. H. Anderson, J. R. Ensher, and E. A. Cornell, Phys. Rev. Lett. **74**, 3352 (1995).

[13] T. H. Bergeman, P. McNicholl, J. Kycia, H. Metcalf, and N. L. Balazs, J. Opt. Soc. Am. B **6**, 2249 (1989).

[14] D. J. Berkeland, J. D. Miller, J. C. Bergquist, W. M. Itano, and D. J. Wineland, J. Appl. Phys. **83**, 5025 (1998).

[15] J. H. Müller, O. Morsch, D. Ciampini, M. Anderlini, R. Mannella, and E. Arimondo, Phys. Rev. Lett. **85**, 4454 (2000).

[16] J. H. Müller, D. Ciampini, O. Morsch, G. Smirne, M. Fazzi, P. Verkerk, F. Fuso, and E. Arimondo, J. Phys. B **33**, 4095 (2000).

[17] K. J. Challis, R. J. Ballagh, and C. W. Gardiner, Phys. Rev. A **70**, 053605 (2004).

[18] S. K. Schnelle, E. D. van Ooijen, M. J. Davis, N. R. Heckenberg, and H. Rubinsztein-Dunlop, Opt. Express **16**, 1405 (2008).

[19] C. Raman, R. Onofrio, J. M. Vogels, J. R. Abo-Shaeer, and W. Ketterle, J. Low Temp. Phys. **122**, 99 (2001).

[20] N. Friedman, L. Khaykovich, R. Ozeri, and N. Davidson, Phys. Rev. A **61**, 031403 (2000).

[21] P. Rudy, R. Ejnisman, A. Rahman, S. Lee, and N. P. Bigelow, Opt. Express **8**, 159 (2001).

[22] K. Henderson, C. Ryu, C. MacCormick, and M. G. Boshier, New J. Phys. **11**, 043030 (2009).

[23] B. Zimmermann, T. Müller, J. Meineke, T. Esslinger, and H. Moritz, New J. Phys. **13**, 043007 (2011).

[24] C. Ryu, K. C. Henderson, and M. G. Boshier, New J. Phys. **16**, 013046 (2014).

[25] C. Ryu and M. G. Boshier, New J. Phys. **17**, 092002 (2015).

[26] C. Ryu, P. W. Blackburn, A. A. Blinova, and M. G. Boshier, Phys. Rev. Lett. **111**, 205301 (2013).

[27] K. O. Roberts, T. McKellar, J. Fekete, A. Rakonjac, A. B. Deb, and N. Kjærgaard, Opt. Lett. **39**, 2012 (2014).

[28] A. B. Deb, T. McKellar, and N. Kjærgaard, Phys. Rev. A **90**, 051401 (2014).

[29] T. A. Bell, J. A. P. Glidden, L. Humbert, M. W. J. Bromley, S. A. Haine, M. J. Davis, T. W. Neely, M. A. Baker, and H. Rubinsztein-Dunlop, New J. Phys. **18**, 035003 (2016).

[30] J. Denschlag, J. E. Simsarian, D. L. Feder, C. W. Clark, L. A. Collins, J. Cubizolles, L. Deng, E. W. Hagley, K. Helmerson, W. P. Reinhardt, S. L. Rolston, B. I. Schneider, and W. D. Phillips, Science **287**, 97 (2000).

[31] O. Morizot, Y. Colombe, V. Lorent, H. Perrin, and B. M. Garraway, Phys. Rev. A **74**, 023617 (2006).

[32] G. R. Dennis, J. J. Hope, and M. T. Johnsson, Comput. Phys. Commun. **184**, 201 (2013).

[33] A. Kumar, R. Dubessy, T. Badr, C. D. Rossi, M. D. G. de Herve, L. Longchambon, and H. Perrin, Phys. Rev. A **97**, 043615 (2018).

[34] M. Modugno, C. Tozzo, and F. Dalfovo, Phys. Rev. A **74**, 061601 (2006).

[35] J. L. Helm, T. P. Billam, A. Rakonjac, S. L. Cornish, and S. A. Gardiner, Phys. Rev. Lett. **120**, 063201 (2018).

[36] Y. J. Lin, A. R. Perry, R. L. Compton, I. B. Spielman, and J. V. Porto, Phys. Rev. A **79**, 063631 (2009).

[37] D. Trypogeorgos, T. Harte, A. Bonnin, and C. Foot, Opt. Express **21**, 24837 (2013).

[38] L. Mathey, A. Ramanathan, K. C. Wright, S. R. Muniz, W. D. Phillips, and C. W. Clark, Phys. Rev. A **82**, 033607 (2010).

[39] See the video in Supplemental Material at http://link.aps.org/supplemental/10.1103/PhysRevA.98.013604 for a visualization of how region boundaries were mapped.

[40] C. S. Chisholm, R. J. Thomas, A. B. Deb, and N. Kjærgaard, arXiv:1805.10574v2.